*Conference on Modelling Fluid Flow (CMFF'25)*
*The 19th International Conference on Fluid Flow Technologies*
*Budapest, Hungary, August 26 - August 29, 2025*

# MULTISCALE COMPUTATIONS OF REACTIVE MULTIPHASE FLOWS

Xiaofei LI, Bingchen LI, Wei CHEN, Junjie LIN, Shuai WANG, Kun LUO*, Jianren FAN

* Corresponding Author. State Key Laboratory of Clean Energy Utilization, Zhejiang University, Hangzhou 310027, P. R. China, E-mail: zjulk@zju.edu.cn

## ABSTRACT

Multiphase reactive flows are essential in energy, chemical, and environmental systems. This paper reviews and compares several multiscale modeling methods for simulating reactive multiphase flows, including particle-resolved direct numerical simulation (PR-DNS), computational fluid dynamics-discrete element method (CFD-DEM), coarse-grained CFD-DEM, multi-phase particle-in-cell (MP-PIC), and coarse-grained computational fluid dynamics -direct simulation Monte Carlo (CFD-DSMC). These methods are assessed for their accuracy, scalability, and computational efficiency in simulating dense gas-solid flows. The developed multiscale models are comprehensively validated against experimental measurements and applied across various scales: microscale simulations of char combustion, mesoscale simulations of particle clusters in coal gasification, macroscale simulations of biomass chemical looping gasification, and industrial-scale applications for coal pyrolysis and combustion staged conversion. This work emphasizes the importance of selecting appropriate modeling strategies for different scales and explores the potential integration of high-performance computing and artificial intelligence to enhance multiscale simulation tools.

**Keywords: Multiphase flow, multiscale simulation, computational fluid dynamics, flow and reaction coupling**

## 1. INTRODUCTION

The dense gas-solid reactive systems are widely present in energy, chemical, and environmental systems (e.g., combustors, gasifiers, reactors, etc.), where complex gas-solid flow, heat and mass transfer, and chemical reactions occur. With the rapid development of computer technology, computational fluid dynamics (CFD) has become an increasingly important complement to both theoretical analysis and experimental research. It effectively addresses the limitations of these two approaches and comprehensively and accurately reproduces the flow, heat transfer, and reactive characteristics of dense gas-solid flows. However, the complex multi-scale nature of dense gas-solid flows, both spatially and temporally, places stringent demands on numerical simulation and necessitates the adoption of appropriate multi-scale solving strategies[1–4].

Depending on the resolution and scale of interest, dense gas-solid reactive systems are commonly modeled by three classic approaches: particle-resolved direct numerical simulation (PR-DNS), computational fluid dynamics-discrete element method (CFD-DEM) under Euler-Lagrange framework, and two-fluid model (TFM) under Euler-Euler framework. In PR-DNS, every particle and the surrounding fluid field are fully resolved, so no closure models are needed to capture fluid motion; this yields outstanding accuracy but comes at the cost of extremely fine grids and correspondingly massive computational resources, which confines PR-DNS to small domains and modest particle counts [5,6]. The conventional CFD-DEM approach within the Euler-Lagrange framework alleviates this burden by allowing grid cells that are roughly three to five times larger than the particles they contain. [7–9]. The gas phase is solved within the Eulerian framework, while the solid-phase particle motion is solved in the Lagrangian framework. The reduction in grid quantity leads to a decrease in computational load. However, the accuracy of gas-phase motion predictions is slightly lower than that of PR-DNS. This method can track each particle individually, providing accurate particle-scale information, which is then interpolated and fed back into the gas-phase grid for further computations. This approach is constrained by particle collision models and grid size requirements and is still mainly applied in laboratory-scale simulations with a limited number of particles[10,11]. By contrast, the two-fluid model (TFM) under Euler-Euler framework adopts the continuous medium assumption, treating the solid phase as a fluid ("pseudo fluid") and solving its motion in the Eulerian framework. The key

challenge of this method lies in modeling the viscosity and pressure of the solid phase, often achieved through the kinetic theory of granular flow (KTGF) [12]. Generally speaking, the can significantly reduce computational load and has been widely used in predicting gas-solid flow within large-scale industrial equipment[13–15]. However, the Euler-Euler method has notable drawbacks: the accuracy of the solid-phase motion is limited to the computational grid scale, preventing the capture of rich particle-scale information. As a result, it is not well-suited for investigating the transport mechanisms of particles in fluidized bed equipment.

In the simulation of multiphase reactive flows, traditional single-scale methods often fail to effectively capture the complex interactions between fluids, particles, and reactions. Multi-scale simulation methods, by considering physical phenomena at different scales, can overcome the limitations of single-scale approaches, significantly improving prediction accuracy and computational efficiency. Specifically, multi-scale simulation methods not only focus on macroscopic flow characteristics but also allow for an in-depth exploration of microscopic particle behavior and chemical reaction mechanisms. This study comprehensively reviews and compares the applicability, accuracy, and scalability of the multiscale numerical simulation methods we have developed in recent years within the Euler-Lagrange framework for modeling multiphase reactive flows, providing essential tools for studying and optimizing these systems.

## 2. MODEL DESCRIPTION

### *2.1 Particle-resolved direct numerical simulation*

In PR-DNS, the gas phase is solved within an Eulerian framework, while the solid phase is tracked using an Lagrangian framework. This approach requires enforcing no-penetration and no-slip boundary conditions on particle surfaces within the computational domain, along with the corresponding heat and mass transfer boundaries. The immersed boundary method with virtual points introduces the effect of particles without requiring mesh reconstruction, instead constructing a virtual embedded boundary through interpolation. The mass conservation equation, momentum conservation equation, energy conservation equation, and species conservation equation for the gas phase are expressed as follows:

$$\frac{\partial \rho}{\partial t} + \nabla \cdot (\rho \mathbf{u}) = 0 \tag{1}$$

$$\rho \frac{\partial \mathbf{u}}{\partial t} + \rho \mathbf{u} \cdot \nabla \mathbf{u} = -\nabla p + \nabla \cdot \tau \tag{2}$$

$$\rho \frac{\partial T}{\partial t} + \rho \mathbf{u} \cdot \nabla T = \sum_k (\dot{\omega}_k - \nabla \cdot \mathbb{J}_k)\left(\frac{TR}{c_y M_k} - \frac{h_k}{c_v}\right) - \frac{\rho TR}{c_v M} \nabla \cdot \mathbf{u} + \frac{\tau^2}{2\mu c_v} - \frac{\nabla \cdot \mathbf{q}}{c_v} \tag{3}$$

$$\rho \frac{\partial Y_k}{\partial t} + \rho \mathbf{u} \cdot \nabla Y_k = -\nabla \cdot \mathbb{J}_k + \dot{\omega}_k \tag{4}$$

where $\rho_f$, $\boldsymbol{u}_f$, and $p_f$ represent the gas phase density, velocity, and pressure, respectively. $\tau_f$ denotes the viscous stress tensor. $T$ represents temperature. $c_v$ is the specific heat at constant volume. $R$ denotes the universal gas constant. $M$ is the molar mass of the gas mixture. $h_k$ denotes the enthalpy of the individual species. $Y_k$ denotes the mass fraction of species $k$. $\dot{\omega}_k$ represents the gas-phase reaction source term for species $k$, and $\mathbb{J}_k$ is the diffusion flux of species $k$.

The principle of the immersed boundary method with virtual points is to designate several layers of grid points near the particle boundary as virtual points (the number of layers is determined by the spatial discretization scheme; in this study, three layers are used). These virtual points are assigned values artificially through interpolation, ensuring that the fluid outside the particle satisfies the corresponding boundary conditions at the particle surface during spatial discretization. At each sub-time step, the assignment of values to the virtual points precedes the solution of the flow field. Mirror points symmetric to the virtual points across the boundary, along with additional auxiliary points on the same side of the interface, are selected to construct interpolation formulas for various boundary conditions, through which the values of the virtual points are determined. The construction of Dirichlet boundary conditions requires only a single mirror point, whereas Neumann and Robin boundary conditions necessitate, in addition to the mirror point, an auxiliary point. Depending on the dimensionality of the case study, the mirror and auxiliary points are obtained using bilinear or trilinear interpolation based on neighbouring grid points. Based on the boundary condition formulation, by specifying appropriate boundary conditions for species balance, velocity, and temperature, accurate simulation of particles can be achieved.

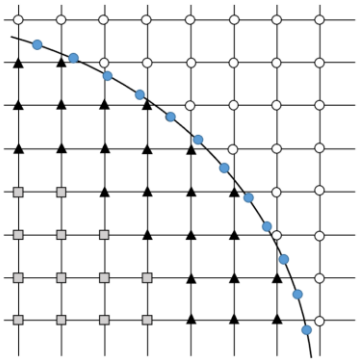

**Figure 1. Schematic diagram of the immersed boundary method with virtual points.**

### *2.2 Euler-Lagrange method*

This section introduces the computational fluid dynamics-discrete element method (CFD-DEM) method, coarse-grained CFD-DEM method, the

multi-phase particle-in-cell method (MP-PIC) method, and the coarse-grained computational fluid dynamics-direct simulation Monte-Carlo (CFD-DSMC) method within the Euler-Lagrange framework, focusing on the governing equations for the gas phase and solid phase, as well as sub-models for particle collisions, heat and mass transfer, and chemical reactions.

### 2.2.1 Gas-phase control equations

The mass conservation equation and momentum conservation equation for the gas phase are expressed as follows:

$$\frac{\partial(\varepsilon_f \rho_f)}{\partial t} + \nabla \cdot (\varepsilon_f \rho_f \boldsymbol{u}_f) = R_f \tag{5}$$

$$\frac{\partial}{\partial t}(\varepsilon_f \rho_f \boldsymbol{u}_{f,i}) + \nabla \cdot (\varepsilon_f \rho_f \boldsymbol{u}_f \boldsymbol{u}_f) = -\varepsilon_f \nabla p + \rho_f \varepsilon_f g + \nabla \cdot (\varepsilon_f \tau_f) - I_{pf} \tag{6}$$

$$\frac{\partial(\varepsilon_f \rho_f C_{p,f} T_f)}{\partial t} + \nabla \cdot (\varepsilon_f \rho_f u_f C_{p,f} T_f) = \nabla \cdot [\varepsilon_f (\kappa_f + \frac{C_{p,f} \nu_{f,t}}{Pr_{T_{f,t}}}) \nabla T_f] - Q_{fp} - \Delta H_{rf} + \gamma_{Rf} (T_{Rf}^4 - T_f^4) \tag{7}$$

$$\frac{\partial(\varepsilon_f \rho_f X_n)}{\partial t} + \nabla \cdot (\varepsilon_f \rho_f u_f X_n) = \nabla \cdot (\varepsilon_f \rho_f D_n \nabla X_n) + R_{fn} \tag{8}$$

where $\varepsilon_f$ represents the gas phase void fraction. $R_f$ and $I_{pf}$ correspond to the mass change source term due to chemical reactions and the interphase momentum exchange source term. $C_{p,f}$, $T_f$, $\kappa_f$, and $\mathrm{Pr}_{f,t}$ represent the specific heat capacity at constant pressure, temperature, thermal conductivity, and Prandtl number of the gas phase, respectively. $Q_{fp}$ denotes the convective heat transfer between the gas and solid phases, $\Delta H_{rf}$ is the heat of reaction, $\gamma_{Rf}$ is the radiative heat transfer coefficient, and $T_{Rf}$ is the radiative temperature of the gas phase. $X_n$ and $D_n$ represent the mass fraction and diffusion coefficient of gas component n, respectively. $R_{fn}$ denotes the mass change due to the chemical reactions involving component n.

### 2.2.2 Solid-phase control equations

In the Lagrangian framework, the motion of particles in the gas-solid flow is obtained by solving Newton's second law. The external forces acting on the particles in the flow field mainly include drag forces induced by fluid-particle interactions, pressure gradient forces, viscous forces, and other forces such as collision forces, viscous forces, and electrostatic forces arising from particle-particle and particle-wall interactions. These external forces allow the determination of particle position, velocity, acceleration, and other related quantities. The equation of motion for the particles can be expressed as:

$$m_p \frac{dv_p}{dt} = m_p g + F_{fp} + F_{drag} + F_c + F_{af} \tag{9}$$

$$I_p \frac{d\omega_p}{dt} = T_p \tag{10}$$

where $m_p$ and $\mathrm{v}_p$ represent the particle mass and velocity, respectively, while $m_p$g, $F_{fp}$, $F_{drag}$, $F_c$, and $F_{af}$ correspond to the gravitational force on the particle, pressure gradient force, drag force, collision force, and additional forces. $I_p$, $\omega_p$, and $\mathrm{T}_p$ represent the particle moment of inertia, angular velocity, and torque, respectively. In the CFD-DEM and coarse-grained CFD-DEM method, the collision force can be resolved by decomposing it into the normal ( $F_{ij}^n$) and tangential ( $F_{ij}^t$) components. In the MP-PIC and CFD-DSMC methods, the collision force is not directly solved but rather modeled through a submodel. The particle collision models for the three methods will be discussed in detail in the following sections.

#### 2.2.2.1 Interphase drag model

The drag force is primarily caused by the velocity difference between the particles and the fluid, and it is the main mechanism for momentum exchange between the particle and gas phases. Therefore, an accurate drag force model is crucial for predicting gas-solid flow processes. For a single particle within a particle group, the drag force it experiences can be calculated as:

$$F_{drag} = \frac{\beta V_p}{1 - \varepsilon_f}(u_f - v_p) \tag{11}$$

where $\beta$ is the interphase momentum exchange coefficient, also known as the drag coefficient, and $V_p$ represents the particle volume. Currently, commonly used drag force models can be broadly classified into the following categories: (i) experimental and empirical models such as the Gidaspow model[16] and the Syamlal-O'Brien model[17]; (ii) models derived from lattice-Boltzmann (LB) and direct numerical simulation (DNS) methods, such as the BVK drag model[18] and the Koch & Hill model[19]; (iii) models based on energy minimization multiscale (EMMS) theory, such as the EMMS drag model[20]. In this study, we primarily use the Gidaspow drag model, which applies to most fluidization calculations, the EMMS drag model that accounts for gas-solid flow heterogeneity, and the BVK drag model with particle size corrections.

#### 2.2.2.2 Particle collision model

In gas-solid flow within a fluidized bed, frequent particle collisions significantly influence particle motion and the flow field distribution. Therefore, accurately calculating particle collisions in numerical simulations is crucial for predicting gas-solid flow behavior in the fluidized bed. Currently, depending on the method used to handle the interparticle interactions, collision models can be broadly classified into two main categories. The first is deterministic methods, which directly compute each particle collision in the computational domain during the simulation process, such as the soft sphere model used in the CFD-DEM and the coarse-grained CFD-DEM method. The second is stochastic methods, which do not directly calculate the particle collisions but instead introduce the concept of collision probability to model them, including the solid-phase stress model applied in the MP-PIC method and the DSMC method.

**(1) Soft-sphere model for CFD-DEM and coarse-grained CFD-DEM**

The soft-sphere model accounts for inter-particle forces during collisions and updates particle positions by computing acceleration, velocity, and displacement based on these forces. Interactions between particles are modeled by incorporating elasticity, damping, and tangential sliding mechanisms. Elasticity captures particle deformation during collisions, damping reflects energy dissipation, and sliding models tangential interactions. In the DEM, the contact force between particles is decomposed into a normal component ($F_{ij}^{n}$) and a tangential component ($F_{ij}^{t}$):

$$F_c = \sum_{j=1, j\neq i}^{N} \left(F_{ij}^{n} + F_{ij}^{t}\right) \tag{12}$$

$$F_{ij}^{n} = -(k_n \delta_n + \eta_n \dot{\delta}_n) n_{ij} \tag{13}$$

$$F_{ij}^{t} = \begin{cases} -(k_t \delta_t + \eta_t \dot{\delta}_t) t_{ij} & |F_{ij}^{t}| \leq \mu |F_{ij}^{n}| \\ -\mu |F_{ij}^{n}| t_{ij} & |F_{ij}^{t}| > \mu |F_{ij}^{n}| \end{cases} \tag{14}$$

where $k$, $\eta$, and $\delta$ represent the elastic stiffness, damping coefficient, and particle deformation displacement, respectively. The subscripts $n$ and $t$ denote the normal and tangential directions. The tangential contact force is constrained by the product of the particle-particle sliding friction coefficient $\mu$ and the normal contact force. If the tangential force exceeds this maximum static friction threshold, sliding occurs between the particles, and the tangential force is subsequently determined based on the sliding friction coefficient.

In traditional CFD-DEM methods, simulating large-scale fluidized bed is often challenging due to the large number of particles in the system, leading to excessive computational load and difficulties in solving the problem. To address this issue, the coarse-graining method is introduced to reduce the number of particles being computed. In the coarse-grained CFD-DEM method, multiple real particles with identical properties are grouped into a single computational particle with an equivalent coarse diameter, thereby reducing the number of particles in the computational domain by a factor of the cube, significantly lowering the computational complexity. The core framework of the coarse-grained CFD-DEM method is the same as that of the traditional CFD-DEM method, still using the soft-sphere model to directly solve the collision process between particles, but in the simulation, coarse particles are used to replace real particles for more efficient computation. The diameter of the coarse particle, $d_{\mathrm{cgp}}$, is given by:

$$d_{cgp} = k d_p \tag{15}$$

where $k$ is the coarse-graining coefficient, and $d_{\mathrm{p}}$ is the diameter of the real particles.

**(2) Solid stress model for MP-PIC**

In the MP-PIC method, a distribution function $f(\mathrm{x}_p, \mathrm{v}_p, m_p, T_p, t)$ is used to describe the distribution of particles in the flow field. This equation is a function of the particle's spatial position, velocity, mass, temperature, and time. The equation is expressed as follows:

$$\frac{\partial f}{\partial t} + \frac{\partial (f v_p)}{\partial t} + \frac{\partial (fA)}{\partial v_p} = \frac{f_D - f}{\tau_D} + \frac{f_G - f}{\tau_G} \tag{16}$$

where $f_D$ and $\tau_D$ represent the particle distribution function and the particle collision relaxation time under local equilibrium conditions, respectively. After a collision, the particle velocity tends to follow an isotropic Gaussian distribution. In this state, $\tau_G$ and $f_G$ denote the relaxation time and the particle distribution function, respectively. A is the particle acceleration, which is expressed as follows:

$$A = \frac{dv_p}{dt} = \beta(u_f - v_p) - \frac{\nabla p}{\rho_p} - \frac{\nabla \tau_p}{\rho_p \varepsilon_p} + g + \frac{\bar{v}_p - v_p}{2\tau_D} \tag{17}$$

where $\bar{\mathrm{v}}_p$ represents the local mass-averaged particle velocity, and $\tau_p$ is the solid-phase stress.

**(3) Collision probability model for coarse-grained CFD-DSMC**

The DSMC method, based on gas molecular kinetics[21], does not directly track the motion of each particle. Instead, it uses probabilistic methods to determine whether collisions occur between particles and employs a relatively small number of sampled particles to represent a large number of real particles. Over a time interval $\Delta t_{\mathrm{p}}$, the collision probability $P_{ij}$ between particle $i$ and particle $j$ within the same grid is given by[21,22]:

$$P_{ij} = \frac{w \pi g_0 (d_{p,i} + d_{p,j})^2 |G_{ij}| \Delta t_p}{4 V_c} \tag{18}$$

where $w$ is the sampling coefficient; $G_{ij}$ is the relative velocity between particle $i$ and particle $j$; and $\mathrm{g}_0$ is the equilibrium spherical radial distribution function at particle contact.

This study proposes the coarsed-grained CFD-DSMC method by coupling the coarse-grained model with the DSMC model. While using collision probability to model the collision process, the method also employs larger computational particles in terms of particle size to further reduce the number of simulated particles. Additionally, the collision probability is modified as follows:

$$P_{ij} = \frac{w \pi g_0 (d_{cgp,i} + d_{cgp,j})^2 |G_{ij}| \Delta t_p}{4 k^3 V_c} \tag{19}$$

#### 2.2.2.3 Particle heat transfer model

Complex heat transfer between the gas and solid phases includes four types of heat transfer: particle-particle conduction, particle-fluid convective heat transfer, radiation heat transfer between particles and their surrounding environment, and the heat of reaction generated by chemical reactions. Particle-particle conduction primarily occurs in regions with high particle concentration and frequent collisions, and, compared to the other types of heat transfer, it accounts for a relatively small portion, often being neglected. Therefore, this study considers only particle-fluid convective heat transfer, radiation heat transfer between particles and their surrounding environment, and the heat of reaction generated by chemical reactions. Under these conditions, the

energy conservation equation for particle $i$ is expressed as:

$$m_{p,i}C_{p,i}\frac{dT_{p,i}}{dt} = Q_{pf,i} + Q_{rad,i} - \Delta H_{r,i} \quad (20)$$

where $C_{p,i}$ is the specific heat capacity of particle $i$, $T_{p,i}$ is the temperature of particle $i$, $Q_{pf,i}$ and $Q_{rad,i}$ represent the convective heat transfer between the particle and the fluid, and the radiative heat transfer between the particle and its surrounding environment, respectively. $\Delta H_{r,i}$ is the heat of reaction.

#### 2.2.2.4 Chemical reaction model

The heterogeneous reactions mainly include evaporation, pyrolysis, gasification, as well as carbonation and calcination reactions of adsorbents. For a specific computational particle, the mass conservation equation considering the mass changes caused by chemical reactions is given by:

$$\frac{dm_p}{dt} = \sum_{n=1}^{N_s} R_{sn} \quad (21)$$

where $N_s$ is the total number of chemical components, and $R_{sn}$ is the mass change rate of component $n$ in the particle due to chemical reactions.

## 3. DISCUSSION AND RESULT

### *3.1 PR-DNS modeling of char combustion at the microscale*

#### 3.1.1 PR-DNS method validation

To verify the reliability of the PR-DNS method, we compared the drag coefficients of cold particles obtained from PR-DNS simulations with the empirical correlation proposed by Schiller and Naumann[16]. The simulation results show good agreement with the empirical formula in Figure 2 (a). Regarding char combustion, simulation results were validated against experimental data from Makino et al.[23] using their experimental configuration, as illustrated in Figure 2 (b). The simulations demonstrate satisfactory agreement with experimental measurements and notably reproduce the important phenomenon observed experimentally: As temperature increases, the dominant reaction shifts. When the $CO_2$-char reaction becomes predominant, it leads to a stepwise decrease in char consumption rate. In conclusion, the PR-DNS method achieves high precision in resolving forces, heat transfer, and mass transfer on particle surfaces, rendering it suitable for the full-scale particle direct numerical simulations conducted in this study.

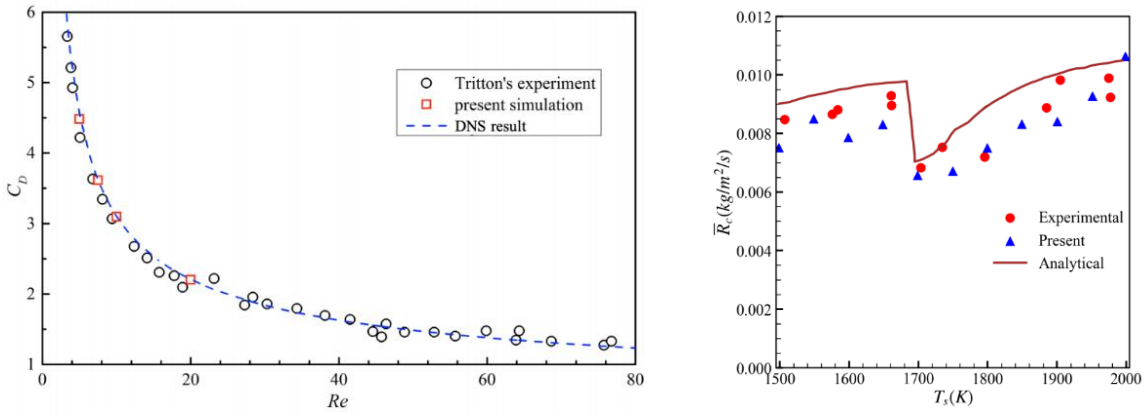


(a) (b)

**Figure 2. PR-DNS method validation: (a) drag coefficient, (b) reaction rate.**

#### 3.1.2 PR-DNS on interaction during the combustion of two char particles

This subsection investigates the mechanistic effects of interactions between burning particles on reaction rates and drag forces. The interparticle interactions are decomposed into three components: wake effects, direct flame interactions between particles, and the nozzle effect arising from interparticle convective flow.

Figure 3 (a) shows the dimensionless drag force at different particle center distances and relative angles. This drag force is normalized by the drag on a single cold-flow particle. Overall, both cold and burning char particles show similar trends when influenced by neighboring particles. The nozzle effect becomes strong only when the line connecting the two particles is near 90 degrees to the flow direction. This causes the drag force to exceed that on a single isolated particle. Figure 3 (b) shows the char reaction rates at different angular positions. These are for center-to-center distances of $l$ = 1.5, 2.0, and 3.0 particle diameters ($D_p$). The reaction rates are normalized by the single particle combustion rate. This normalization uses identical inflow conditions. In all cases except the side-by-side case at $l = 3.0D_p$, the carbon consumption rate is lower than for an isolated particle. As particle separation increases, the particles move from dense to sparse arrangements. During this process, the reaction rates gradually increase. Meanwhile, the

effects of wake flow and trailing flames progressively decrease.

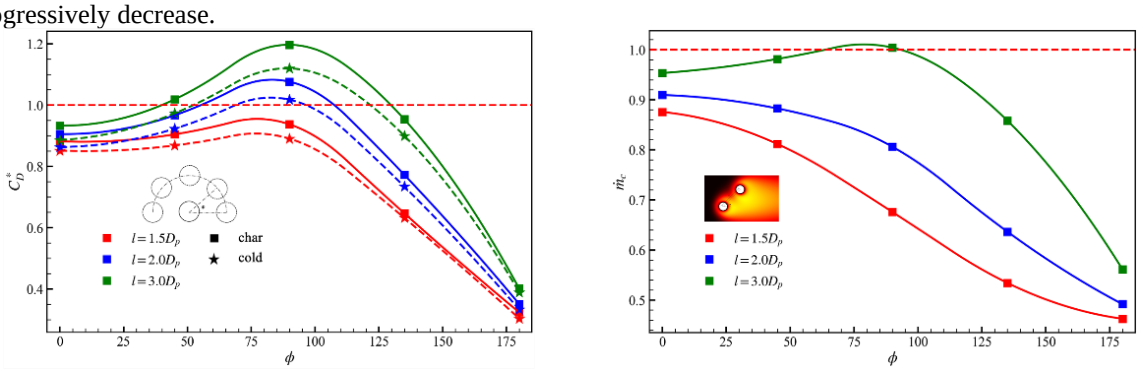


(a) (b)

**Figure 3. The interaction during the combustion of two char particles: (a) drag coefficient distribution, (b) reaction rate distribution.**

When studying how two-particle interactions affect reaction rates, we find that the nozzle effect has little influence on char reaction rates. Convection contributes almost nothing to species transport around particles. This is shown in Figure 4 and Figure 5. These figures display $O_2$ and CO transport budgets along the axis between side-by-side particles. Flame interaction is confined to boundary layers. Therefore, no direct flame interaction occurs when particle separation exceeds $2D_p$. The interactions between particles mainly affect forces through nozzle effects and wake flows. We also compared the drag coefficients of burning and cold-flow particles. This comparison shows that particle interaction effects on reaction rates cannot be directly applied to correct drag coefficients. Particle interactions remain dominant in controlling these forces.

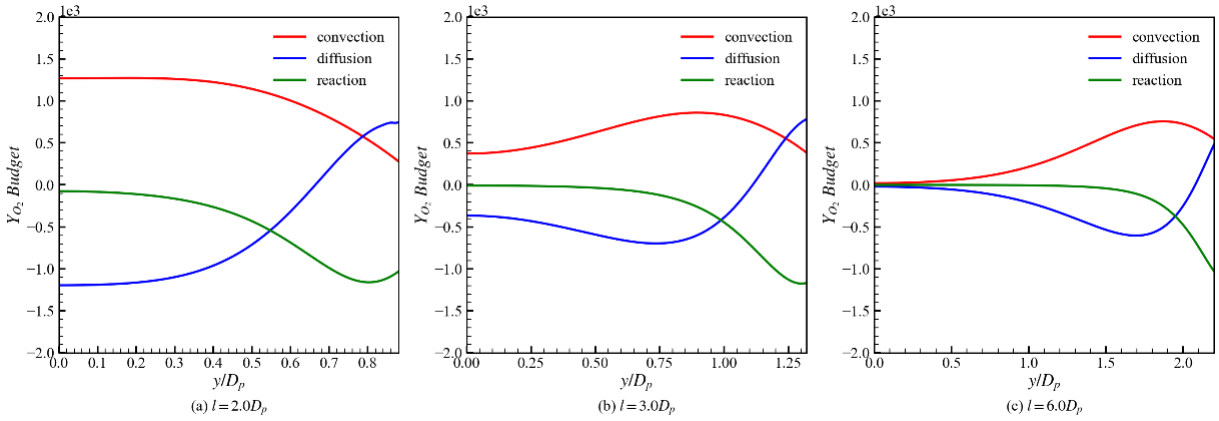


**Figure 4. $O_2$ transport budget analysis between two char particles**

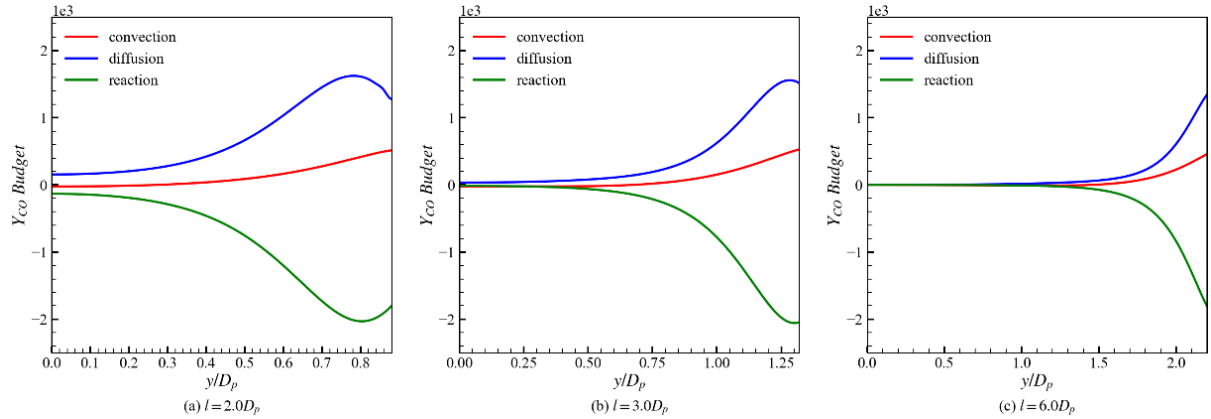


**Figure 5. CO transport budget analysis between two char particles**

### *3.2 CFD-DEM and coarse-grained CFD-DEM simulation of particle cluster behavior in coal gasification at the mesoscale*

The presence of particle clusters in the riser of a circulating fluidized bed significantly affects the overall performance of the reactor. This study conducts in-depth investigations into the behavior of particle agglomerates in a riser adopting CFD-DEM and coarse-grained CFD-DEM simulations based on the Euler-Lagrange framework.

First, CFD-DEM simulations were performed on the characterization of particle clusters in laboratory-scale risers referring to Carlos Varas et al. [24] and compared with the longitudinal distribution curves of time-averaged particle concentrations, as shown in Figure 6 (a). The simulation results are in good agreement with the experimental data. It was observed that the overall particle concentration within the riser increases, and particles primarily accumulating in the lower region of the riser. Figure 6 (b) further compares the horizontal distribution of particle concentration at a gas velocity of 5.95 m/s, showing that the predicted results closely match the experimental values in both trends and magnitudes.

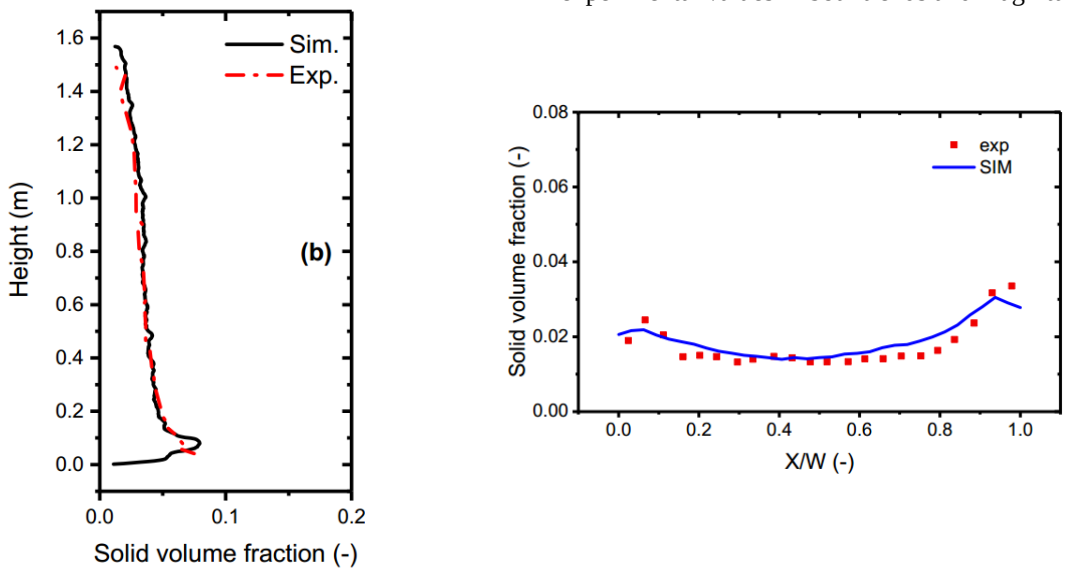


(a) (b)

**Figure 6. (a) Comparison between the predicted particle volume concentration and time-averaged measured values; (b) Horizontal distribution of particle volume concentration.**

Furthermore, coarse-grained CFD-DEM is adopted to simulate a larger-scale fluidized bed reactor. The molar ratios of gas products at the riser outlet were statistically analyzed over 15s-30s, as shown in Figure 7 (a). It is observed that, although there are slight fluctuations in the CO to $CO_2$ ratio, the overall gasification product ratio remains relatively stable after 15s. Moreover, the outlet component data was time-averaged and compared with experimental data, as shown in Figure 7 (b). It was found that the particle size distribution of the bed material and fuel had relatively little impact on the component distribution at the outlet. Under all operating conditions, the simulated predictions closely match the experimental measurements, demonstrating that the coarse-grained CFD-DEM method can accurately predict the component distribution at the outlet.

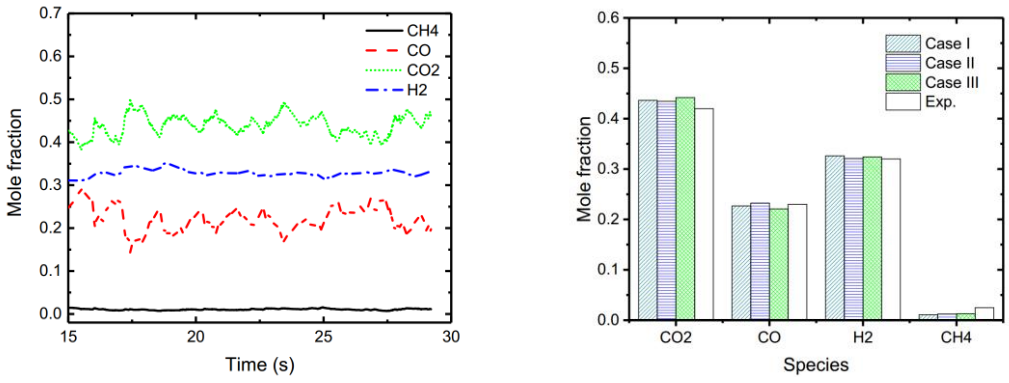


(a) (b)

**Figure 7. (a) Temporal variation of gas product ratios at the outlet; (b) Comparison of gas product ratios at the outlet under different operating conditions.**

To gain a fundamental understanding of the fluidization characteristics within the riser, time-averaged results are presented in Figure 8. It is observed that the horizontal solid-phase concentration distribution within the bed exhibits a typical ring-core structure. In the vertical direction, as the height increases, the particle concentration decreases, and the high-concentration region near the wall accordingly shrinks.

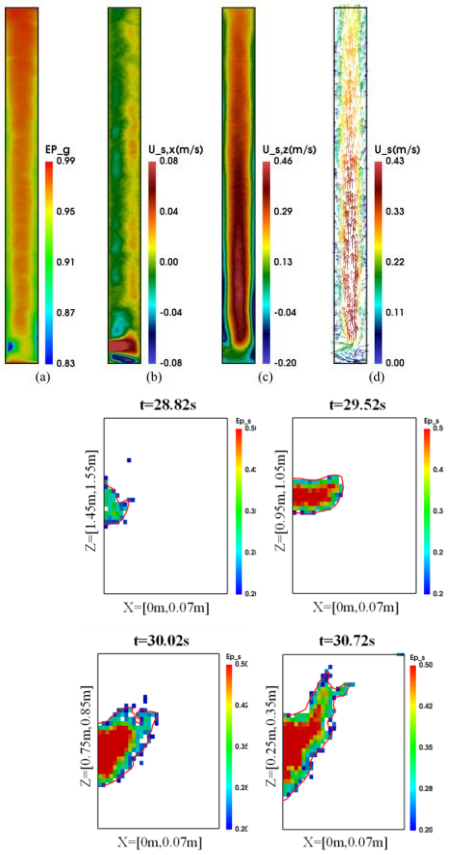


**Figure 8. Time-averaged gas-solid flow characteristics: (a) fluid voidage; (b) solid horizontal velocity; (c) solid vertical velocity; (d) solid velocity vector distribution.**

Figure 9 provides a comprehensive summary of the intrinsic mechanisms underlying the temporal evolution of particle clusters. The analysis highlights the influence of the tail effect of the particle cluster on its formation. By tracking the dynamic evolution of a typical particle cluster, it was found that the characteristics of the cluster exhibit a quasi-periodic variation pattern. The changes in the properties of the particle cluster are primarily attributed to the interactions between the cluster and its surrounding environment. The competition and coordination between the growth and fragmentation mechanisms of the particle cluster lead to a strong correlation between its various characteristics (such as area, width, and falling velocity).

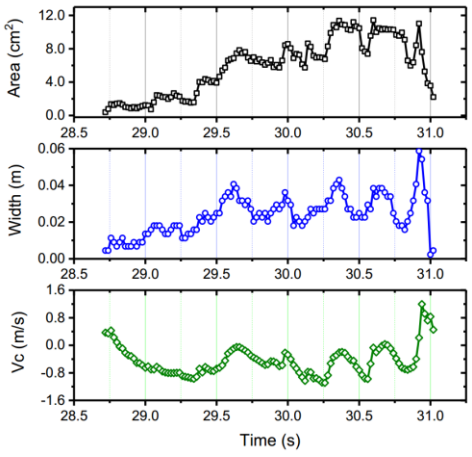


(a) (b)

**Figure 9. Particle cluster behavior: (a) evolution of flow pattern; (b) temporal evolution curve.**

### *3.3 Multiphase CFD-DSMC simulations of biomass chemical looping gasification at the macroscale*

To simultaneously meet the requirements of both computational time and accuracy, a CG CFD-DSMC model was developed by coupling the coarse-graining method with the DSMC method. This model enhances computational efficiency while ensuring accuracy by employing collision probabilities and reducing the number of computational particles. The gasifier reactor from the dual-fluidized bed gasification system at Zhejiang University was selected as the simulation object. Figure 10 presents the gas product component concentrations at the gasifier outlet, as predicted by different simulation methods, alongside experimental results. It can be observed that CO and $H_2$ account for the majority of the gas composition at the gasifier outlet. The relative error between the simulated outlet gas concentrations and the experimental results is less than 20%, indicating that the errors in both methods are within an acceptable range. Compared to the MP-PIC method, the CG CFD-DSMC method demonstrates superior control of both the average and maximum errors in the prediction of gas component concentrations at the outlet.

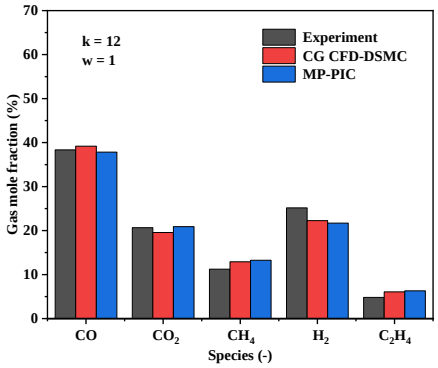


**Figure 10. Concentration of gas product components at the outlet simulated by different methods.**

Furthermore, based on the 1 $MW_{th}$ pilot-scale BFB-CFB dual-fluidized bed system, a comparative simulation analysis of the biomass chemical-looping gasification process was conducted using the CG CFD-DSMC method proposed in this study and the traditional MP-PIC method. Figure 11 presents the average gas product component concentrations at the gasifier outlet. It can be observed that the computational accuracy and efficiency of the two models are approximately equivalent.

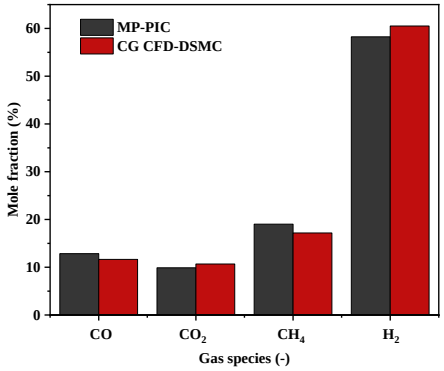


**Figure 11. Gas product component concentrations at the gasifier outlet simulated by MP-PIC and CG CFD-DSMC method.**

After ensuring the accuracy and efficiency of the model, a simulation study on the operational optimization of the structurally optimized biomass chemical-looping gasification system was conducted. Figure 12 presents the axial distribution characteristics of the biomass particle heat transfer coefficient (HTC) under different average particle sizes. The results indicate that the HTC of biomass particles is relatively high near the feed inlet and gradually decreases along the axial direction. This is primarily due to the continuous reduction in the temperature gradient between the biomass particles and the surrounding environment during the heat exchange process after the particles enter the gasifier. It is noteworthy that although the distribution trend of HTC is similar across different particle size conditions, the average absolute value of HTC decreases as the absorber's average particle size increases, suggesting a negative impact on the heat transfer process.

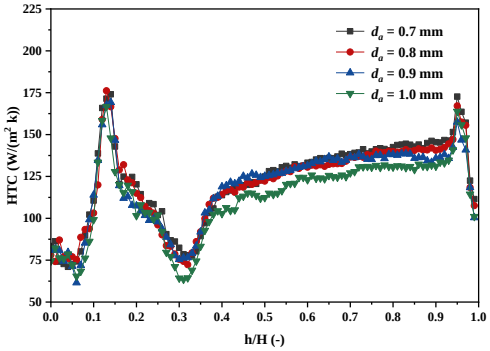


**Figure 12. Effect of the average particle size on the heat transfer coefficient of biomass particles.**

Figure 13 (a) illustrates the effect of biomass feed inlet height on the gas product composition. As the feed inlet height increases, the concentrations of CO and $CO_2$ in the outlet gas gradually increase, while the $H_2$ concentration significantly decreases. Simultaneously, the height of the gas-solid reaction zone increases with the feed inlet height, leading to reduced contact efficiency between $CO_2$ and bed material particles, thus affecting the carbonation reaction. After entering the gasifier, biomass particles undergo a series of physical and chemical transformations, causing a reduction in their mass. Some biomass particles are carried away by the gas flow after staying in the gasifier for a certain period. Therefore, a lower feed inlet height can extend the residence time of biomass particles in the gasifier, enhancing the gas-solid mixing effect and improving carbon conversion efficiency. Figure 13 (b) shows the effect of feed inlet height on LHV and CGC, where both LHV and CGC decrease as the feed inlet height increases, negatively impacting gasification efficiency.

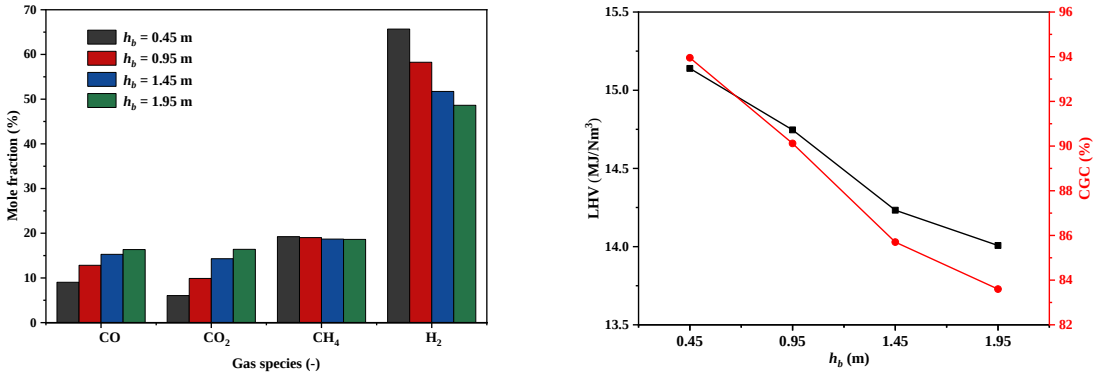


(a) (b)

**Figure 13. Effect of biomass feed inlet height on gasification performance: (a) gas product components at the outlet; (b) LHV and CGC.**

### *3.4 Industrial-scale MP-PIC simulation of coal pyrolysis and combustion staged conversion*

The numerical model is extended to 150 MWe industrial-scale equipment and verifies the applicability of the model at industrial scale by simulating the cold and hot states of large existing equipment at Shanxi Power Plant. Figure 14 presents a comparison between the numerical simulation results and experimental data for the time-averaged normalized molar fractions of each gas component at the cyclone separator outlet of the pyrolysis furnace. The error between the simulation results and experimental data for $CH_4$ and $H_2$ is within 5%, while for $CO_2$, CO, and $C_2H_6$, the error is within 20%, which is acceptable in engineering applications.

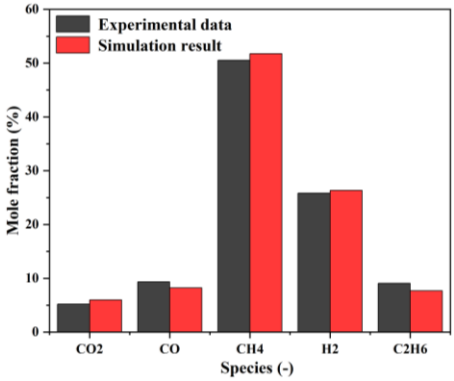


**Figure 14. Comparison of simulated results and experimental data for the molar fractions of each gas component at the cyclone separator outlet of the pyrolysis furnace over time.**

Figure 15 presents the simulation results, experimental data, and relative errors for the time-averaged syngas density at the cyclone separator outlet of the pyrolysis furnace at different operating temperatures. The trend of gas component content variation with temperature is consistent with engineering practice, and the simulation results closely match the experimental data. Monitoring the time-averaged syngas density at the pyrolysis furnace outlet and converting it to the density under standard conditions, the error in syngas density is within 3% at all temperatures. Overall, the model is reliable for predicting the flow regime and thermo-chemical properties of the circulating fluidized bed coal classification pyrolysis combustion integrated multi-product system.

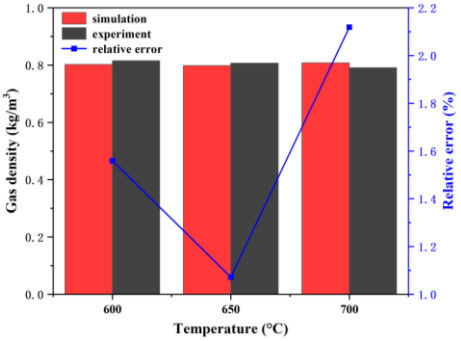


**Figure 15. Comparison of time-averaged syngas density at the cyclone separator outlet of the pyrolysis furnace at different operating temperatures.**

Based on the 150 MWe large-scale coal pyrolysis combustion classification conversion dual fluidized bed system at the Shanxi Pinglu Power Plant, the gas-solid flow field information inside the furnace was obtained using a cold-state model. Figure 16 shows the transient particle distribution in the system at different primary air velocities in the combustion furnace, with particle residence time represented by color. It can be observed that as the primary air velocity in the combustion furnace increases, the load on the four cyclone separators of the combustion furnace intensifies. Particularly at 15 m/s, a large number of particles clog the return feed pipes connecting the cyclone separators to the combustion furnace's bottom, which will impact the normal operation of the system. In contrast, the particle amount in the two small cyclone separators on the combustion furnace side connected to the pyrolysis furnace shows minimal variation. Therefore, changes in the primary air velocity of the

combustion furnace have a relatively small effect on the operation of the pyrolysis furnace side.

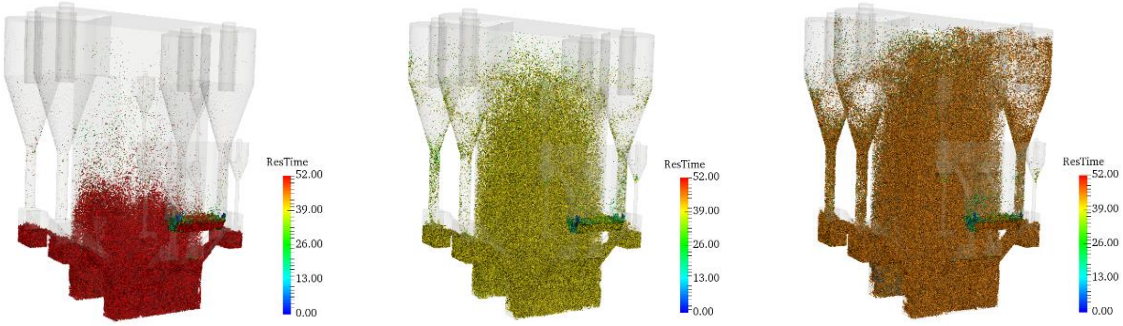


(a) (b) (c)

**Figure 16. Transient particle distribution in the system at different primary air velocities in the combustion furnace: (a) 5 m/s; (b) 10 m/s; (c) 15 m/s.**

Next, the temperature, gas composition, and particle distribution were obtained using a hot-state model to provide theoretical support for the system's design modifications. After the hot-state model reached dynamic stability, the distribution of particle volume fraction in the system was obtained, as shown in Figure 17 (a). It can be seen that the particle accumulation at the inclined surface of the feed leg, which was difficult to avoid in the cold-state model, has disappeared in the hot-state model, and the height of the high particle volume fraction area in the feed leg has decreased. The operation of the return feeders is stable, with sufficient particle accumulation effectively isolating the gas environments of the two furnaces, enabling material circulation between the furnaces while preventing gas backflow. The mass flow rates of syngas components at the pyrolysis furnace cyclone separator outlet were extracted, and the time-averaged molar fractions of the stable pyrolysis furnace circulating syngas components are shown in Figure 17 (b). The highest proportion is $CH_4$, close to 50%, followed by $H_2$ at about 25%, and then $CO_2$, CO, and $C_2H_6$ in decreasing order. Compared to the 1 MWth coal dual fluidized bed pyrolysis combustion classification conversion pilot plant, changes in the circulating syngas components were observed after the pyrolysis furnace stabilized. This suggests that compared to the pyrolysis furnace with single-sided coal feeding and sand as bed material, the system in this chapter involves some coal being fed directly from the combustion furnace and using coal particles generated ash as bed material, which led to significant changes in several characteristics.

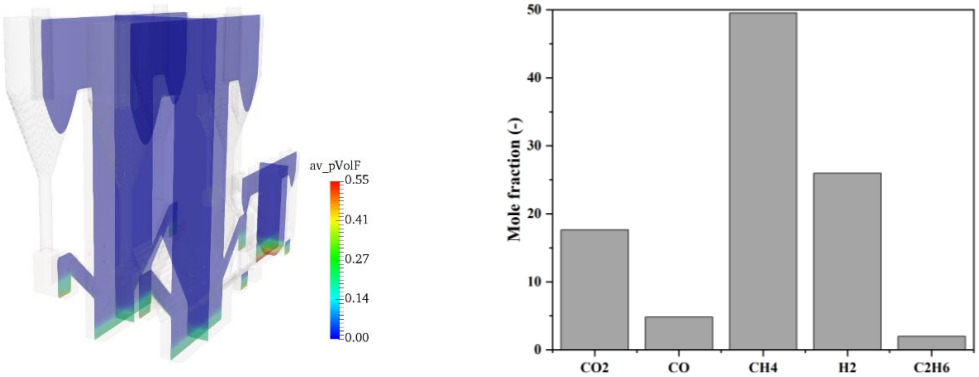


(a) (b)

**Figure 17. (a) The distribution of the time-averaged particle volume fraction at each central cross-section; (b) the time-averaged molar fractions of each gas component at the cyclone separator outlet of the pyrolysis furnace.**

## 4. CHALLENGES AND OUTLOOK

The various multiscale modeling methods reviewed in this paper each have distinct advantages and limitations depending on the scale and complexity of the system. At the microscale, the PR-DNS delivers unparalleled accuracy in resolving particle–fluid interactions and surface transport phenomena, yet its exorbitant mesh requirements confine it to small domains. Moreover, methods such as traditional CFD-DEM and its coarse-grained variant alleviate this burden by coupling continuum fluid solvers with discrete particle tracking, achieving reasonable precision while remaining

computationally tractable. For systems dominated by gas-phase transport, the coarse-grained CFD-DSMC and MP-PIC approaches scale efficiently to larger volumes, enabling practicale engineering simulations where computational efficiency becomes paramount.

A key challenge lies in the trade-off between model accuracy and computational efficiency. As the complexity of the simulations increases, the computational demand grows significantly. High-performance computing (HPC) and artificial intelligence (AI) integration offer great potential to accelerate multiscale simulations. AI can assist in optimizing models, improving computational strategies, and automating parameter adjustments. However, integrating AI with traditional physical models remains a challenge.

Looking ahead, a unified framework for multiscale coupling is essential. Such a framework would facilitate seamless integration across different scales, enhancing both accuracy and efficiency. Additionally, building a platform that combines data-driven approaches with physical modeling will be critical in advancing the next generation of simulation tools. This unified approach will offer more accurate, scalable, and efficient simulations, crucial for tackling complex engineering systems in the future.

## ACKNOWLEDGEMENTS

We are grateful for the supports from the Fundamental Research Funds for the Central Universities (Grant No. 226-2024-00138), National Natural Science Foundation of China (Grant No. 588020-X42405), National Key Research and Development Plan of China (Grant No. 2024YFB4105902), Key Research and Development Program of Zhejiang Province (Grant No. 2025C01047), and Xplorer Prize.

## REFERENCES

[1] Norouzi H R, Zarghami R, Sotudeh-Gharebagh R, et al. Coupled CFD-DEM modeling: formulation, implementation and application to multiphase flows[M]. John Wiley & Sons, 2016.

[2] Sundaresan S, Ozel A, Kolehmainen J. Toward Constitutive Models for Momentum, Species, and Energy Transport in Gas-Particle Flows[J]. Annual Review of Chemical and Biomolecular Engineering, 2018, 9: 61-81.

[3] Tenneti S, Subramaniam S. Particle-Resolved Direct Numerical Simulation for Gas-Solid Flow Model Development[J]. Annual Review of Fluid Mechanics, 2014, 46: 199-230.

[4] Van Der Hoef M A, Van Sint Annaland M, Deen N G, et al. Numerical simulation of dense gas-solid fluidized beds: a multiscale modeling strategy[J]. Annual Review of Fluid Mechanics, 2008, 40: 47-70.

[5] Luo K, Tan J, Wang Z, et al. Particle-resolved direct numerical simulation of gas-solid dynamics in experimental fluidized beds[J]. AIChE Journal, 2016, 62(6): 1917-1932.

[6] Tang Y, Lau Y M, Deen N G, et al. Direct numerical simulations and experiments of a pseudo-2D gas-fluidized bed[J]. Chemical Engineering Science, 2016, 143: 166-180.

[7] Clarke D A, Sederman A J, Gladden L F, et al. Investigation of Void Fraction Schemes for Use with CFD-DEM Simulations of Fluidized Beds[J]. Industrial & Engineering Chemistry Research, 2018, 57: 3002-3013.

[8] Freireich B, Kodam M, Wassgren C. An exact method for determining local solid fractions in discrete element method simulations[J]. Aiche Journal, 2010, 56: 3036-3048.

[9] Peng Z, Doroodchi E, Luo C, et al. Influence of void fraction calculation on fidelity of CFD-DEM simulation of gas-solid bubbling fluidized beds[J]. Aiche Journal, 2014, 60: 2000-2018.

[10] Li C, Eri Q. Comparison between two Eulerian-Lagrangian methods: CFD-DEM and MPPIC on the biomass gasification in a fluidized bed[J]. Biomass Conversion and Biorefinery, 2023, 13(5): 3819-3836.

[11] Singh R I, Brink A, Hupa M. CFD modeling to study fluidized bed combustion and gasification[J]. Applied Thermal Engineering, 2013, 52(2): 585-614.

[12] Gidaspow D. Multiphase flow and fluidization: continuum and kinetic theory descriptions[M]. Academic press, 1994.

[13] Adamczyk W P, Kozołub P, Kruczek G, et al. Numerical approach for modeling particle transport phenomena in a closed loop of a circulating fluidized bed[J]. Particuology, 2016, 29: 69-79.

[14] Hamidouche Z, Masi E, Fede P, et al. Unsteady three-dimensional theoretical model and numerical simulation of a 120-kW chemical looping combustion pilot plant[J]. Chemical Engineering Science, 2019, 193: 102-119.

[15] Lu B, Zhang N, Wang W, et al. 3-D full-loop simulation of an industrial-scale circulating fluidized-bed boiler[J]. Aiche Journal, 2013, 59: 1108-1117.

[16] Gidaspow D. Multiphase Flow and Fluidization: Continuum and Kinetic Theory Descriptions[M]. Academic Press, 1994.

[17] Syamlal M, O'Brien T J. The derivation of a drag coefficient formula from velocity-voidage correlations[J]. Technical Note, US Department of Energy, Office of Fossil Energy, NETL, 1987.

[18] Beetstra R, Van Der Hoef M A, Kuipers J. Drag force of intermediate Reynolds number flow past mono-and bidisperse arrays of spheres[J]. AIChE Journal, 2007, 53(2): 489-501.
[19] Hill R J, Koch D L, Ladd A J. Moderate-Reynolds-number flows in ordered and random arrays of spheres[J]. Journal of Fluid Mechanics, 2001, 448: 243-278.
[20] Li J, Cheng C, Zhang Z, et al. The EMMS model—its application, development and updated concepts[J]. Chemical Engineering Science, 1999, 54(22): 5409-5425.
[21] Bird G A. Molecular Gas Dynamics[M]. Oxford, 1976.
[22] Huilin L, Zhiheng S, Ding J, et al. Numerical simulation of bubble and particles motions in a bubbling fluidized bed using direct simulation Monte-Carlo method[J]. Powder Technology, 2006, 169(3): 159-171.
[23] Makino A, Namikiri T, Kimura K. Combustion rates of graphite rods in the forward stagnation field with high-temperature airflow[J]. Combustion and Flame, 2003, 132(4): 743-753.
[24] Kraft S, Kuba M, Kirnbauer F, et al. Optimization of a 50 MW bubbling fluidized bed biomass combustion chamber by means of computational particle fluid dynamics[J]. Biomass and Bioenergy, 2016.